ADVANCED FUNCTIONAL MATERIALS
www.afm-journal.de

AlScN-on-SiC Thin Film Micromachined Resonant Transducers Operating in High-Temperature Environment up to 600 °C

*Wen Sui, Haoran Wang, Jaesung Lee, Afzaal Qamar, Mina Rais-Zadeh, and Philip X.-L. Feng**

The experimental demonstration of aluminum scandium nitride (AlScN)-on-cubic silicon carbide (SiC) heterostructure thin film micromachined resonant transducers operating in a high-temperature environment up to 600 °C is reported. Macroscopic and microscopic vibrations are investigated through a combination of ultrasensitive laser interferometry techniques and Raman spectroscopy. An average linear temperature coefficient of resonance frequency (TC*f*) of <1 ppm °C^{-1} within the temperature range from room temperature to 200 °C, and an average linear TC*f* of –16 ppm °C^{-1} between 200 and 600 °C, from the fundamental-mode resonance of AlScN/SiC circular diaphragm resonator with a thickness of 1.9 µm and diameter of 250 µm, is obtained. Higher-order modes exhibit much larger TC*f*, which make them strong candidates as high-temperature-tolerant temperature sensors or ultraviolet detectors. Raman spectroscopy indicates that the turning points of the peak positions of the longitudinal optical phonon modes of both 3C-SiC and AlScN occur in almost the same temperature region where the turnover point of TC*f* is observed, suggesting that the microscopic vibrations in the crystal lattice and the macroscopic oscillation of the diaphragm are naturally mediated by the residual strain inside the materials at varying temperature.

1. Introduction

Microelectromechanical systems (MEMS) offer shrinking size, weight, and power alternatives to the commercial off-the-shelf sensors and systems, which make them attractive for a variety of important applications ranging from communication, biomedical, automotive, to military and aerospace environments.[1–6] Conventional silicon (Si) MEMS sensors are not suited for harsh environment applications due to the failing of Si electronics at ≈350 °C and degradation of Si mechanical properties at a temperature above 500 °C.[7] However, different sectors, from industry to space, are in great need of sensors that are capable of operating in harsh environments, and sometimes at extreme temperatures, high radiation levels, and/or in corrosive gases.[8–10] As a result, researchers have looked into materials, which are intrinsically more tolerant to these extreme cases. Wide-bandgap materials, such as III-nitrides, silicon carbide (SiC), and diamond-like carbon (DLC) have emerged as promising alternatives beyond Si, for MEMS to operate in harsh environments due to their superior electronic, mechanical, thermal, and chemical properties.[11–13] Among them, sputter-deposited aluminum nitride (AlN) has attracted great attention for radio frequency (RF) applications due to its high acoustic phase velocity, low motional resistance, and CMOS compatibility.[14] As a nonferroelectric material, the piezoelectricity of AlN is limited by the critical temperature at which the chemical bonds break down, rather than by the Curie point.[15] AlN has been reported to maintain its piezoelectricity at temperatures up to 1150 °C.[16] When scandium (Sc) is added to AlN, the piezoelectric coefficient gradually increases with the Sc concentration up to ≈40%, from ≈5pCN^{-1} up to ≈25pCN^{-1}.[17] The high piezoelectricity of aluminum scandium nitride (AlScN) is persistent up to at least 600 °C (no degradation in its d_{33} coefficient), making AlScN an appealing candidate for sensor material at elevated temperatures.[18] However, it still presents a major challenge for growing high-quality AlScN thin films on Si due to the large lattice mismatch and different thermal expansion.[19,20]

Due to the large lattice mismatch of 19% between AlN and Si, it is possible to generate a highly dislocated region within a few hundred nanometers from the interface if AlN is grown directly on a Si substrate.[21] In addition, the large thermal expansion coefficient (TEC) mismatch between AlN and Si may lead to an increase in the curvature of the stack at elevated temperatures.[22] If the stress of the substrate (which can exhibit bowing or warping) exceeds the strength of the AlN layer, it will have cracks. To mitigate this issue, 3C-SiC, which possesses a

W. Sui, H. Wang, J. Lee, P. X.-L. Feng
Department of Electrical and Computer Engineering
Herbert Wertheim College of Engineering
University of Florida
Gainesville, FL 32611, USA
E-mail: philip.feng@ufl.edu
A. Qamar, M. Rais-Zadeh
Department of Electrical Engineering & Computer Science
University of Michigan
Ann Arbor, MI 48109, USA
M. Rais-Zadeh
NASA Jet Propulsion Laboratory
California Institute of Technology
Pasadena, CA 91109, USA
The ORCID identification number(s) for the author(s) of this article can be found under https://doi.org/10.1002/adfm.202202204.

DOI: 10.1002/adfm.202202204

comparable lattice constant and a matching TEC with those of AlN, has been used as the intermediate layer on top of Si, for the deposition of high-quality AlN films.[23] It has been reported that the introduction of the 3C-SiC layer reduces the lattice mismatch from 19% to 1%, and TEC mismatch from 47% to 18%, respectively.[24] Sc doping with a concentration <20% has no significant effect on the lattice constant of AlN,[25] which makes it possible to grow high-quality crystalline AlScN on 3C-SiC and help reduce the energy dissipation and improve the quality factors (*Q*s) of resonant MEMS.[26] Additionally, SiC has drawn great attention as a structural material for harsh environment applications due to its outstanding mechanical and chemical properties, specifically high hardness, wear resistance, mechanical robustness, good thermal stability, and corrosion resistance.[27] In terms of electronic properties, compared to Si, SiC exhibits a larger bandgap (2.3–3.4 eV), a higher breakdown field (3 MV cm^{-1}), and a high saturation velocity (2×10^7 cm s^{-1}).[28] In addition, single-crystalline SiC can be grown on large area substrates and is compatible with batch manufacturing processes used in the Si micromachining and integrated circuit (IC) industries.[29]

Recent development in coupling AlN and SiC offers exciting opportunities for building MEMS operating in high-temperature environments, so as to possibly combine the high-temperature-durable piezoelectricity of AlN and the commercial availability of 3C-SiC wafers as well as advanced micromachining techniques.[6,30] Thanks to the excellent acoustic wave guiding of AlScN-on-SiC (or simply AlScN/SiC) heterostructure, surface acoustic wave (SAW) delay lines fabricated on AlScN/SiC have been demonstrated, which exhibit high SAW velocities >12 000 m s^{-1}, much higher than counterpart AlScN SAW devices on Si substrate.[31] It has been reported that using AlScN/SiC as the device layer also improves the overall thermal performance of the MEMS and leads to higher RF power handling.[32,33] Although AlScN alloy thin films exhibit a good balance between high tolerable temperature and strong piezoelectricity,[18] AlScN/SiC thin film micromachined resonant transducers operating in high-temperature environment have not been explored. How the change of temperature affects the intrinsic properties of AlScN/SiC composite thin film is still unexplored, and remains an open question in the field.

Before adding electrodes and utilizing the expected strong piezoelectricity of AlScN, it is important to understand and verify the high-temperature stability of the AlScN/SiC heterostructure MEMS, and to calibrate evolution of crystal quality with increased temperature. Here, we investigate and demonstrate AlScN/SiC thin film micromachined resonant transducers operating in high-temperature environment up to 600 °C. We employ ultrasensitive optical interferometry techniques to measure the resonance frequencies of the AlScN/SiC thin film resonators without any metal electrodes, which can rule out the effects of electrode via degradation at high temperature. Raman spectroscopy is used to investigate the temperature-dependent microscopic vibrations in AlScN/3C-SiC diaphragm resonators. The investigation of both device-level and atomic level vibrations in AlScN/3C-SiC diaphragm resonators at varying temperatures could provide insight into analyzing how temperature fluctuations affect the intrinsic material properties of AlScN/3C-SiC thin film, and further open an avenue toward the high-temperature tolerant temperature sensors or ultraviolet (UV) detectors based on AlScN/SiC thin film micromachined transducers.

2. Scientific Background and Experimental Design

Figure 1a,c show an optical microscopy image of an AlScN/SiC diaphragm released from the substrate with a diameter $d = 500$ µm in the front side view and an scanning electron microscope (SEM) image of the etched cavity in the backside view, respectively. Optical microscopy images of the fabricated AlScN/SiC diaphragms with different diameters (d = 250, 500, 750, and 1000 µm) indicate that large diaphragms are likely to be buckled, due to the built-in stress generated in the sputtered AlScN film. As will be discussed later, the built-in stress plays an important role in defining the resonant characteristics of AlScN/SiC diaphragm resonators at elevated temperatures. Figure 1b shows the transmission electron microscope (TEM) image of the AlScN/SiC interface, which shows the columnar growth of AlScN; no grain boundaries are observed in the 3C-SiC thin film and the most of defects are stacking faults.[30] Both the XRD pattern and selected area electron diffraction pattern of the AlScN/3C-SiC/Si heterostructure confirm that the 3C-SiC thin film and AlScN thin film are single crystalline and polycrystalline, respectively (see Figures S1,S2, Supporting Information). A previous report on AlN/SiC MEMS resonator suggests that the degraded quality factor (Q) with temperature originates from metal electrodes via degradation with temperature, carbon contamination from testing in the open air, and probes shifting due to thermal expansion.[6] To avoid these issues and better understand the mechanical properties of pristine AlScN/SiC heterostructure at high temperatures up to 600 °C, the resonances of the AlScN/SiC diaphragm resonators without depositing any metal electrodes are characterized in moderate vacuum (≈50 mTorr) by an ultrasensitive laser interferometry system configured with a precisely temperature-controlled stage. The Raman measurement system is integrated into the laser interferometry system, as shown in Figure 1d (see Methods section). The diagram illustrated in Figure 1e displays the analyzed effects of varying temperatures on the resonance frequency.

3. Temperature-Dependent Multimode Resonances

Figure 2 shows the multimode resonances of a AlScN/SiC device with a diameter of 250 µm measured at varying temperature. We carefully adjust the position of the red laser to detect more resonance modes, simultaneously. Totally four resonance modes are observed at 25 °C (room temperature) in the range of 700 to 1000 kHz, specifically, f_1 = 788 kHz, f_2 = 827 kHz, f_3 = 850 kHz, f_4 = 899 kHz (Figure 2a). To study the resonance of AlScN/SiC diaphragm at high temperatures, we characterize the temperature coefficient of resonance frequency (TCf) of the four resonance modes starting from 25 up to 600 °C. Figure 2b,c shows the resonance spectra of the four modes measured as a function of temperature for both the

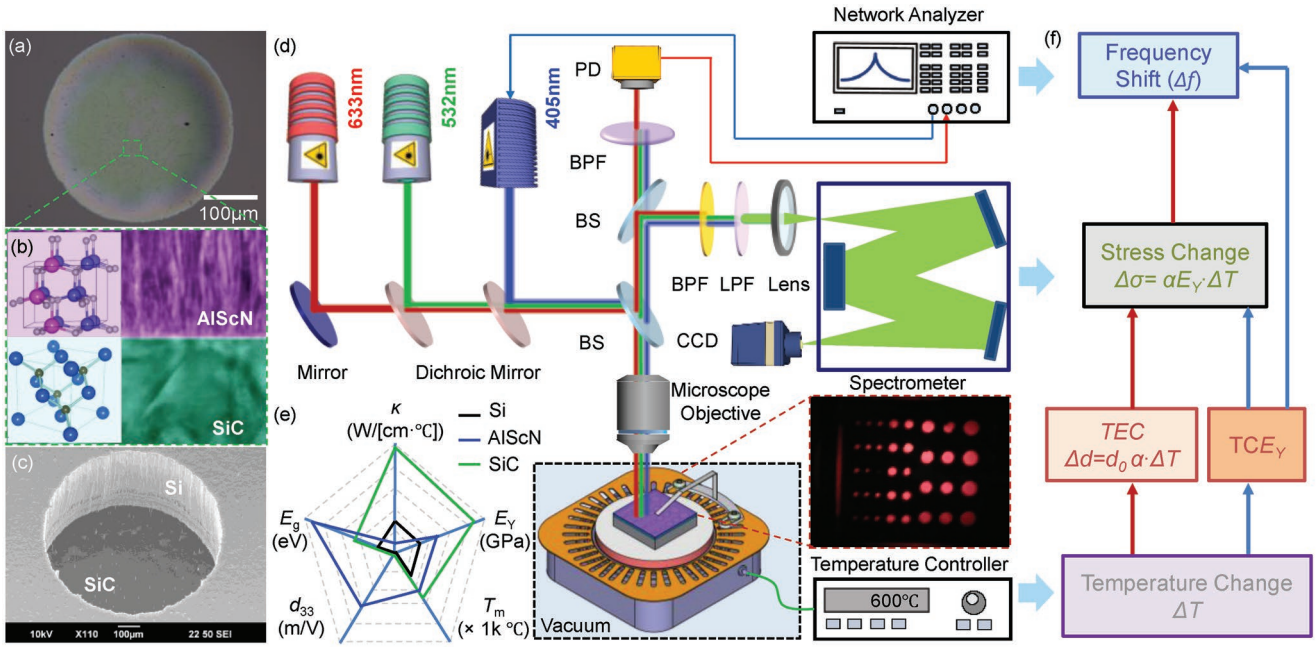

Figure 1. Scientific background and experimental design. a) Optical image of a fabricated AlScN/3C-SiC circular diaphragm resonator with $d = 500$ µm in the front side view. b) TEM cross-sectional image of the AlScN/3C-SiC interface. c) SEM image of the etched cavity with $d = 500$ µm in the backside view. d) Illustration of the combined Raman spectroscopy/interferometry measurement system configured with a precisely temperature-controlled device stage. BPF, LPF, PD, and BS represent a band-pass filter, a long-pass filter, a photodetector, and a beam splitter, respectively. e) Comparison between key material properties of Si, 3C-SiC, and AlScN. f) Block diagram showing effects of varying temperature on the resonance frequency. TCE_Y is the temperature coefficient of Young's modulus, α is the tehrmal expansion coefficient, d_0 represents the initial diameter before temperature change.

heating (ramp up) and cooling (ramp down) periods. Interestingly, the resonance frequency increases when the temperature is changed from room temperature to 100 °C and then decreases slightly with increasing temperatures for the 1st mode (Figure 2d), while monotonic increase of frequency is observed in 2nd, 3rd, and 4th mode in the same temperature range (Figure 2e–g). The temperature dependence is even more significant when the temperature is above 400 °C. Compared to higher-order modes, the 1st order mode shows a smaller TCf, with resonance frequency slightly decreasing from ≈788 kHz at 25 °C to ≈784 kHz at 600 °C. Overall, we observe clear consistency in resonances for all the four modes measured during heating and cooling processes, validating the AlScN/SiC diaphragm resonators can operate reliably at high temperatures up to 600 °C without degradation.

To better understand the multimode frequency response to temperature, we plot the frequency shift at different temperatures with respect to its resonance frequency at room temperature for each mode (see **Figure 3**a–d). As can be seen in Figure 3a, the fractional frequency shift of the 1st mode is completely different from that of any other mode. Specifically, we observe almost constant $\Delta f/f$ values within the temperature range from ≈25 to 200 °C, with an average TCf of less than 1 ppm °C^{-1}. This is due to second order characteristic of the resonance frequency shift with temperature with a turn-over point of 100 °C at which point the TCf is zero. Such a small TCf value (high-temperature stability) is desirable and promising to enable stable MEMS resonators for frequency reference and timing applications. However, when the temperature is above 200 °C, we observe a linear downshift relation between $\Delta f/f$ and T, with an average TCf of –16 ppm °C^{-1}. This level of temperature stability of the AlScN/SiC diaphragm resonator is better than MEMS resonators based on AlN or 3C-SiC.[34–37] With proper thermal compensation design, material engineering, and/or geometry engineering, it is possible to achieve zero TCf in AlScN/SiC diaphragm resonator for frequency reference applications in high temperature and harsh environments.[38]

Interestingly, higher-order modes present different frequency responses, in which two segments of linear upshift of fractional frequency are observed within the measured temperature range, as shown in Figure 3b–d. At lower temperatures, below 200 °C, the average TCf of all the modes are calculated between 80 and 140 ppm °C^{-1}, which is about 1/3 of that measured in higher temperature region above 200 °C, with the average TCf between 250 and 400 ppm °C^{-1}. To better understand the evolution of TCf with temperature, we calculate the TCf at each temperature point by using the resonance frequencies measured at two adjacent temperatures (see Figure 3e–h). TCf values of each of the four modes show modest change when the temperature is below 200 °C, which indicates that the mechanical properties of the as measured AlScN/SiC diaphragm resonator are thermally stable. Subsequently, a linear increase of absolute TCf values is observed as the temperature increases up to ≈500 °C. Note that a turn-over point occurs in the TCf plot for all the four modes at ≈500 °C, above which the absolute TCf values decrease with temperature increase up to 600 °C. As will be discussed later, such complicated variation of TCf is determined by the competing effects of built-in stress, Young's modulus as well as thermal expansion properties. Figure 3i–l shows the Q as a function of temperature for both the heating and cooling processes. As

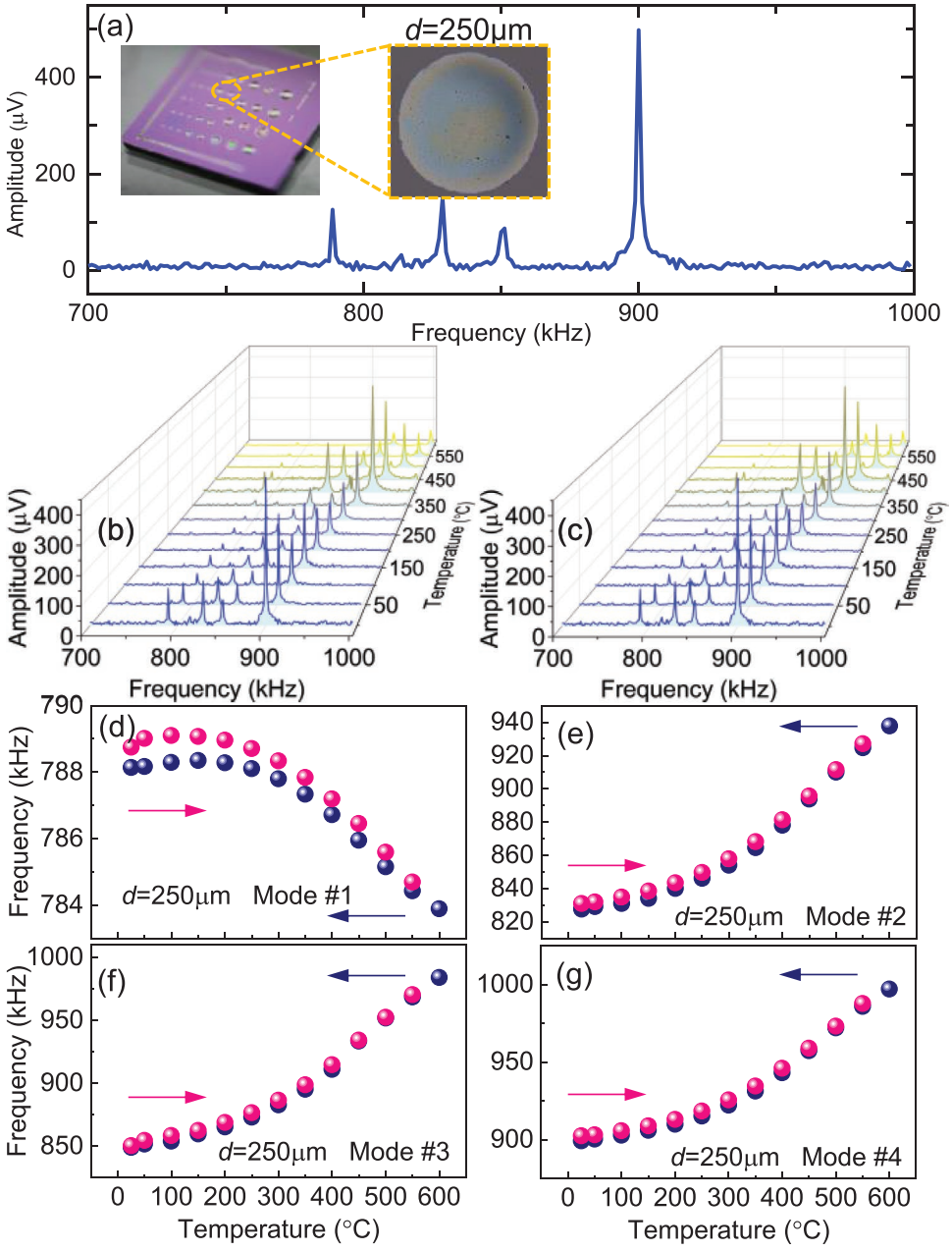

Figure 2. Measured temperature-dependent multimode resonances for an AlScN/SiC MEMS resonator with $d \approx 250$ µm. a) Multimode resonance spectra measured at room temperature (25 °C). Inset shows the chip photo and an optical image of the measured AlScN/SiC circular diaphragm resonator in the front side view. b) Multimode resonance spectra measured with increasing temperature from 25 up to 600 °C (Heating). c) Multimode resonance spectra measured with decreasing temperature from 600 to 25 °C (Cooling). Measured temperature-dependent resonance frequencies for the d) 1st, e) 2nd, f) 3rd, and g) 4th mode. Pink arrows indicate the heating process while the blue arrows indicate the cooling process.

expected, Q degrades with temperature, which may result from the energy dissipation from the thermoelastic damping due to the temperature gradient in the heterostructure and/or intrinsic material loss from phonon-phonon interactions.[38]

To further understand the frequency response of AlScN/SiC circular diaphragm resonators at varying temperature, we measure the multimode TCf of a AlScN/SiC device with the largest diameter of 1000 µm on the same chip. We characterize the TCf of the first three resonance modes measured in the range of 30–350 kHz, with f_1 = 64 kHz, f_2 = 253 kHz, f_3 = 296 kHz (**Figure 4**a,b). We plot the frequency shift at different temperatures with respect to its resonance frequency at room temperature for each mode in Figure 4c–e. The fundamental mode shows positive TCf with two segments of linear upshift of fractional frequency. When the temperature is below 300 °C, the average TCf is ≈60 to 70 ppm °C^{-1}, which is 1/2 of that measured in higher temperature region above 300 °C with the average TCf of ≈150 ppm °C. However, the 2nd mode shows negative TCf, in which two segments of linear downshift of fractional frequency are observed in Figure 4d. In low-temperature

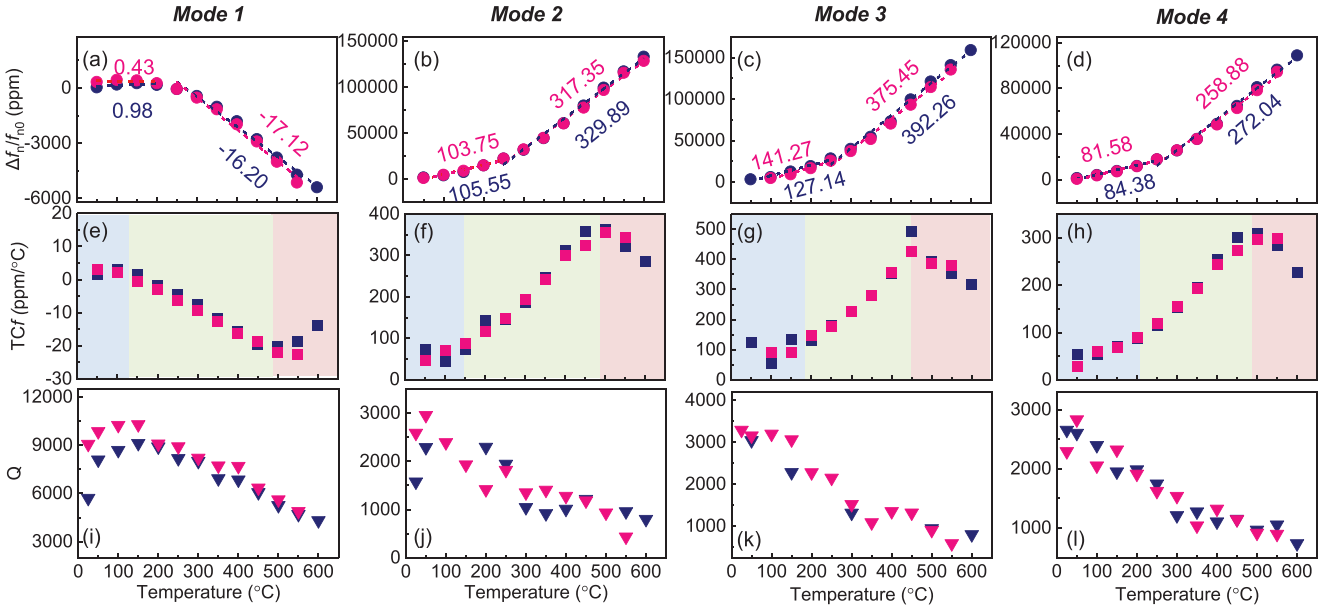

Figure 3. Measured multimode TCf for an AlScN/SiC resonator with a diameter $d \approx 250$ µm. a–d) Fractional frequency shift ($\Delta f_n/f_{n0}$) with varying temperature for the three modes, where reference frequency f_{n0} is the frequency measured at room temperature. The averaged TCf is obtained by linear fitting of the $\Delta f_n/f_{n0}$ versus temperature plot. e–h) TCf versus temperature, where the TCf at different temperatures is calculated by $TCf(T) = (1/f(T)) \times (\Delta f/\Delta T)$. i–l) Measured Q as a function of temperature for both the heating and cooling processes.

region (below 300 °C), the average TCf is about −30 to −50 ppm °C^{-1}. After that, a transition occurs between 300 and 350 °C, and a much larger TCf of about −370 ppm °C^{-1} is obtained when the temperature is higher than 350 °C. For the third mode, a linear upshift of fractional frequency leads to an average TCf of ≈90 ppm °C^{-1} as the temperature increases up to 450 °C. However, a turnover of TCf from positive to negative occurs between 450 and 500 °C, which may result from the thermal instability caused by the change of stress distribution inside the heterostructure. Similar to the characteristics observed in the smaller devices, the Q degrades with temperature for all three modes (Figure 4i–k).

The multimode resonance frequency of circular diaphragm resonators can be expressed as[39]

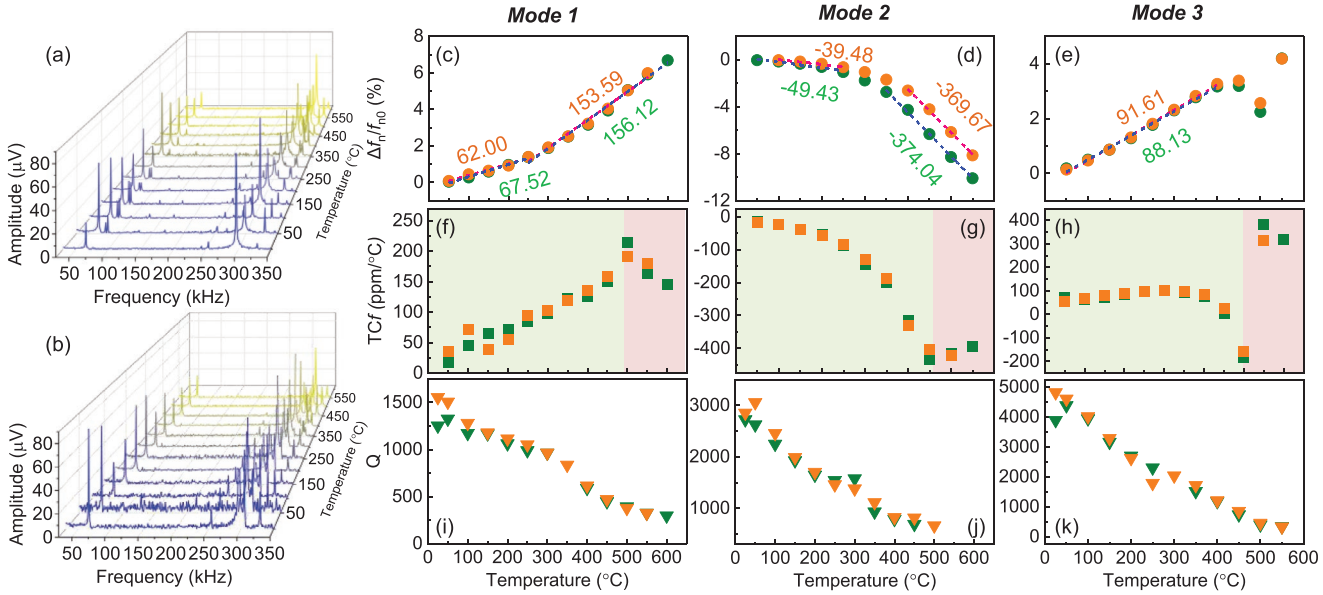

Figure 4. Measured temperature-dependent multimode resonances for an AlScN/SiC diaphragm resonator with the diameter $d \approx 1$mm. a) Multimode resonance spectra measured with increasing temperature from 25 °C up to 600 °C. b) Multimode resonance spectra measured with decreasing temperature from 600 to 25 °C. c–e) Fractional frequency shift ($\Delta f_n/f_{n0}$) with varying temperature for the three modes, where reference frequency f_{n0} is the frequency measured at room temperature. The averaged TCf is obtained by linear fitting of the $\Delta f_n/f_{n0}$ versus temperature plot. f–h) TCf versus temperature. i–k) Measured Q as a function of temperature for both the heating and cooling processes.

$$f_n = \left(\frac{k_n r}{2\pi}\right)\sqrt{\frac{D}{\rho t r^4}\left[(k_n r)^2 + \frac{\gamma r^2}{D}\right]} \quad (1)$$

where n denotes the mode number, ρ is the material mass density, t is the device thickness, $(k_n r)^2$ is the numerically calculated modal parameter, r is the radius of circular diaphragm, γ refers to the built-in tension (in [N/m], or stress [N/m^2 or Pa] times thickness), and D is the flexural rigidity, $D = E_Y t^3/[12(1\text{-}\nu^2)]$ in which E_Y and ν are Young's modulus and Poisson's ratio, respectively. **Equation 1** yields a mixed elasticity model, in which both flexural rigidity (dominated by the thickness and elastic modulus) and built-in tension (stress) play key roles in determining the resonance frequency. When $\gamma r^2/D$ is very large and dominates in Equation 1, Equation 1 goes in the membrane regime, in which the frequency is dominated by the built-in tension. The TCf of tension dominant limit case can be derived as

$$(TCf)_n \approx \frac{\alpha}{2} - \frac{\alpha E_{Y0}}{2\sigma_0} \quad (2)$$

where α refers to the TEC, σ_0 is the initial reference temperature, and E_{Y0} is Young's modulus at reference temperature.

As $\gamma r^2/D$ goes very small and negligible in Equation 1, flexural rigidity dominates the frequency, i.e., and the model approaches the plate regime. The TCf in the flexural rigidity dominant limit can be derived as

$$(TCf)_n \approx \frac{3}{2}\alpha + \frac{TCE_Y}{2} \quad (3)$$

where TCE_Y refers to the temperature coefficient of Young's modulus.

The detailed derivation of the TCf for both the membrane regime and plate regime are illustrated in the Section S3, Supporting Information. Because the multimode resonance frequencies of our AlScN/SiC resonators cannot be fitted well by either membrane model or plate model, our devices are operating in the transition region between these two regimes. The intricate variation of TCf with temperature observed in Figures 3 and 4 can be ascribed to the intricate competing effects of temperature-induced changes in TEC, built-in stress, and Young's modulus. The difference in the TCf values among different modes may be the result of the different temperature dependence of the spatial stress profiles mediated by the different mode shapes. The integral of the position-dependent stress over the entire mode shape leads to different overall stress that modifies the resonance frequency of each mode. The temperature dependency of such behavior is mode-dependent, thus yielding different TCf values for different modes.

4. Temperature-Dependent Raman Characterization

Raman scattering spectroscopy is a nondestructive technique, which can provide valuable information on the vibrational characteristics of materials.[40,41] To better understand the microscopic vibrations in the crystal lattice at varying temperature, we use Raman spectroscopy to study the optical phonon characteristics in both the "as grown" unetched AlScN/SiC region and the self-supported "free-standing" AlScN/SiC window, where the Si substrate is etched, yielding a comparison of Raman spectra from the stressed AlScN/SiC heterostructure and unstressed AlScN/SiC heterostructure grown under the exact same conditions. The typical Raman spectra of AlScN/SiC sample measured at room temperature and higher temperature up to 600 °C from both unetched region and Si-etched region are illustrated in **Figure 5**, in which Si, AlScN, and SiC Raman spectra are recorded simultaneously. As can be seen in Figure 5a, the room temperature Raman spectra measured on unetched AlScN/SiC/Si region show a clear Si peak at ≈520 cm^{-1}, and the spectral bands peaking at around 796 and 973 cm^{-1} correspond to the transverse optical (TO) and the longitudinal optical (LO) phonon modes of 3C-SiC, respectively.[42,43] Note that the LO phonon peak of 3C-SiC clearly possesses a shoulder at 940–950 cm^{-1}, but this feature seems not to affect the LO line. Though there are some bumps on the spectra that might correspond to the Raman peak of AlScN, we are not able to decide their position exactly due to their low intensity. In contrast, the room-temperature Raman spectra measured from the Si-etched window region show clear peaks at 646 and 876 cm^{-1} corresponding to the E_2(high) and A_1(LO) phonon modes of AlScN,[44,45] with the full width at half maximum (FWHM) of 29 and 20 cm^{-1}, respectively. Compared to the Raman spectrum of pure AlN, the incorporation of Sc leads to a redshift and broadening of the Raman modes, which indicates a softening of the lattice and an increased scattering rate of the optical phonons. This can be ascribed to the decrease

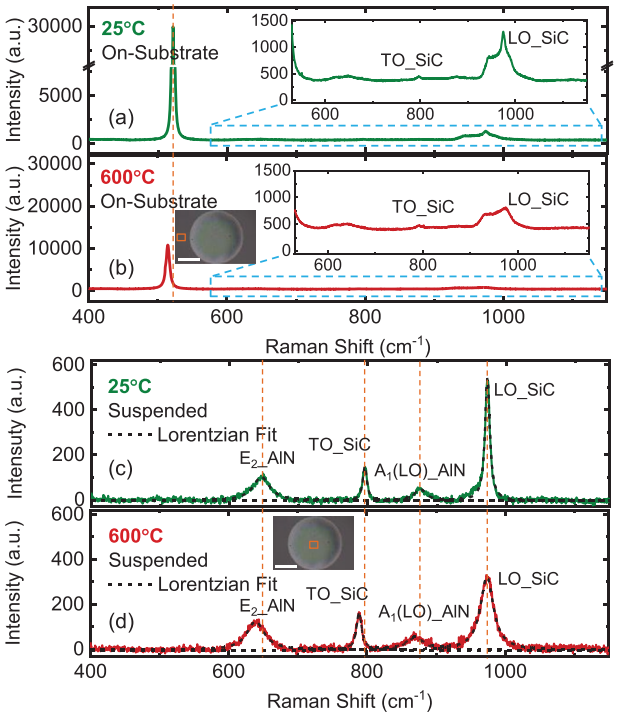

Figure 5. Raman spectra of on-substrate AlScN/SiC measured at a) 25 °C and b) 600 °C. Raman spectra of suspended AlScN/SiC measured at c) 25 °C and d) 600 °C. Insets show the optical microscopy images, with the colored box showing the location where data are taken. Lorentzian Fitting is shown for data in a–d). Scale bars: 100 µm.

of covalent bond strength and the increase of average atomic mass by replacing Al with Sc atoms.[46] Similar to the SiC Raman spectra taken from unetched region, the positions and FWHM values derived by Lorentz fitting are 795 and 7.1 cm^{-1} for TO phonon mode and 973 and 8.3 cm^{-1} for LO phonon modes (Figure 5c). Interestingly, compared to the spectra measured from the unetched AlScN/SiC/Si region, there is no shoulder at 940–950 cm^{-1} from the spectra measured from the Si-etched AlScN/SiC window region. Such feature may be correlated with the interface states between the 3C-SiC layer and the Si substrate.[47,48] As the temperature increases up to 600 °C, a softening (redshift) of the phonon frequencies is observed for both Si phonon mode and two phonon modes of AlScN. However, the TO phonon mode and LO phonon mode of SiC show opposite response to thermal heating, namely a redshift for TO mode and a blueshift for LO mode. As will be discussed later, such different temperature response characteristics of the Raman modes indicate the intricate microscopic vibration of atoms, which further dominates the macroscopic vibration of the AlScN/SiC diaphragm resonator by mediating the stress of the composite structure.

Figure 6 illustrates the Raman spectroscopy results of unetched AlScN/SiC region measured at varying temperatures. Within the temperature range between 25 and 600 °C, the Raman peak positions of Si redshift and the line widths broaden with increasing temperature. The temperature-dependent Raman peak center and FWHM are related to anharmonic terms in the potential energy of atomic vibration, which were approximated by the following Balkaski theory equation[49]

$$\omega(T) = \omega_0 + C\left(1+\frac{2}{e^x-1}\right) + D\left(1+\frac{3}{e^x-1}+\frac{3}{(e^x-1)^2}\right) \quad (4)$$

$$\mathrm{FWHM}(T) = A\left(1+\frac{2}{e^x-1}\right) + B\left(1+\frac{3}{e^x-1}+\frac{3}{(e^x-1)^2}\right) \quad (5)$$

with

$$x = \frac{hc\omega_{(T=0)}}{2k_BT} \quad (6)$$

and

$$y = \frac{hc\omega_{(T=0)}}{3k_BT} \quad (7)$$

Here, A, B, C, and D are anharmonic constants. Parameters x and y are two constants related to temperature. h is Planck's constant, c is the speed of light in vacuum, k_B is Boltzmann constant, and $\omega_{(T=0)}$ is optical phonon frequency at 0 K with a value of 525 cm^{-1}. As can be seen from Figure 6, there is a discrepancy between the Balkaski theory curve and our results, which indicates that the temperature effect is not the only role dominating the position and FWHM of Si Raman peak. Both the spatial confinement effect and mechanical stress originated from the lattice distortion can also influence the peak position.[50] Unlike other Raman experiments performed at different temperatures using laser heating, we utilize a heating stage to heat the device directly from the backside. The different heating efficiency between the two methods may also induce discrepancies on the shift of Raman peak. As will be detailed later, higher heating efficiency can be achieved through mounting chips by using clamps with lower thermal conductivity. Figure 6e–h shows the Raman spectra measured at varying temperatures on unetched AlScN/SiC region. Though the accurate peak positions of SiC are hard to determine, it is clear that thermal

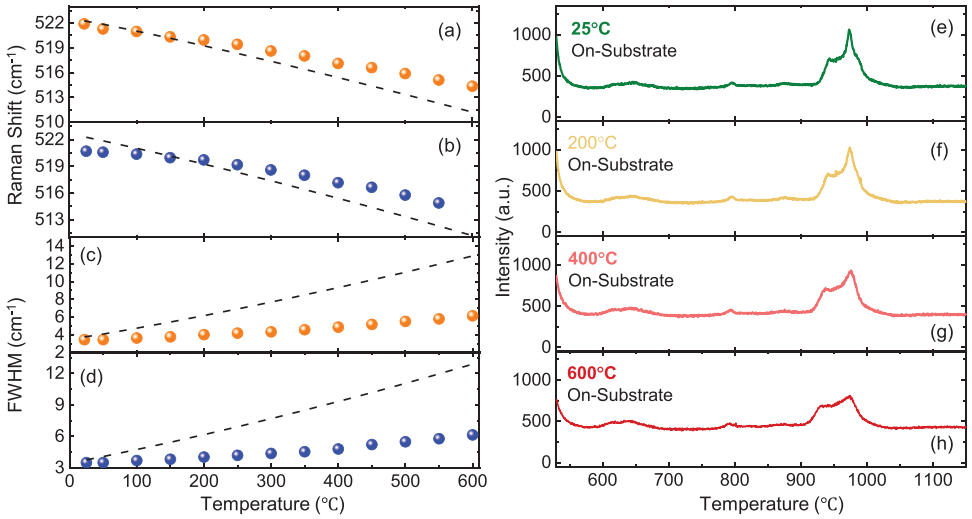

Figure 6. Raman spectroscopy results of on-substrate AlScN/SiC measured at varying temperatures. Evolution of Si Raman mode with temperature a) increasing from 25 to 600 °C and b) decreasing from 600 to 25 °C. Evolution of the FWHM of Si Raman mode with temperature c) increasing from 25 to 600 °C and d) decreasing from 600 to 25 °C. The dashed lines in Figure 6a–d show the temperature-dependent of peak positions and FWHM of crystalline Si calculated by Balkaski theory equation, with ω_0 = 528 cm^{-1}, A = 1.295 cm^{-1}, B = 0.105 cm^{-1}, C = –2.96 cm^{-1}, and D = –0.174 cm^{-1}. Raman spectra of unetched AlScN/SiC measured at e) 25 °C, f) 200 °C, g) 400 °C, and h) 600 °C.

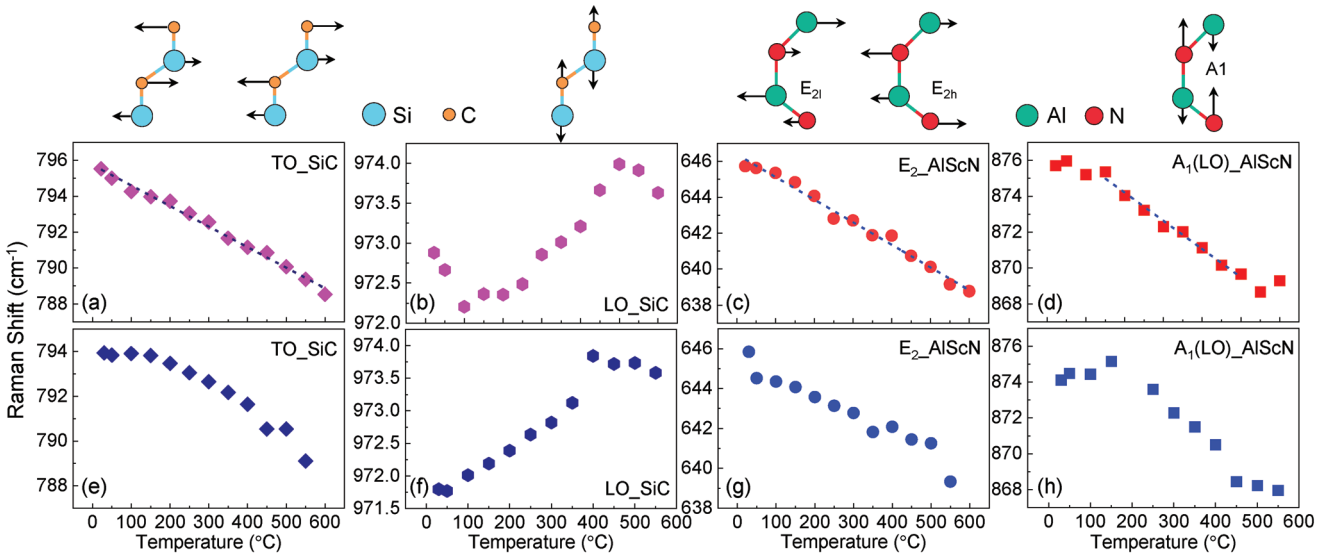

Figure 7. Raman spectroscopy results of suspended AlScN/SiC heterostructure measured at varying temperatures. Temperature dependence of the peak position of a) TO_SiC mode, b) LO_SiC mode, c) E_2_AlScN mode, and d) A_1(LO)_AlScN mode with temperature increasing from 25 to 600 °C. Temperature dependence of the peak position of e) TO_SiC mode, f) LO_SiC mode, g) E_2_AlScN mode, and h) A_1(LO)_AlScN mode with temperature decreasing from 600 to 25 °C.

heating leads to the peak broadening and decreases the peak intensity.

Figure 7a,b shows the TO and LO mode peak positions of the 3C-SiC as a function of temperature. Overall, the TO Raman peak position is more sensitive to the temperature variation in comparison with that of the LO peak. For one, this may be related to the anisotropic stress field distribution in 3C-SiC layer originated from the lattice mismatch and difference in the thermal expansion coefficients between 3C–SiC and Si. For another, this may be ascribed to the anisotropic stress relaxation, i.e., there is only one preferential stress relaxation direction.[47] Within the temperature range between 25 and 600 °C, a linear decrease with increasing temperature is observed for the TO mode, with the temperature coefficient of the first-order Raman peak defined as TCR_a of 1.15×10^{-2} cm^{-1} K^{-1}. However, the LO mode first redshifts with temperature increasing from 25 to ≈100 °C and then blueshifts linearly with temperature increasing to ≈400 °C. Note that the LO mode of 3C-SiC redshifts again as the temperature further increases up to 600 °C. Interestingly, the turning point of the peak position of the LO mode of 3C-SiC occurs at almost the same temperature as the turnover point of TCf (Figure 3). This indicates that the microscopic vibrations in the crystal lattice at varying temperatures dominates the macroscopic vibration of the diaphragm. The absolute shift of peak centers of E_2 and A_1 mode of AlScN induced by temperature is shown in Figure 7c,d,g,h, respectively. The peak centers of E_2 mode show a strictly linear dependence on temperature, with TCR_a of 1.26×10^{-2} cm^{-1} K^{-1}. We observe linear relation between the shift of A_1 mode and T among most of the measured temperatures, from ≈100 to ≈400 °C. In this range, we extract an average TCR_a of 1.571×10^{-2} cm^{-1} K^{-1}. Similar to what has been observed in the LO mode of 3C-SiC, there are two turning points, appearing near the two ends of the temperature range for the A_1 mode of AlScN, which is typically used to characterize the residual stress in AlScN. It is reasonable to claim that the shift of resonance frequency with temperature can be attributed to the change of residual stress within the AlScN/SiC stack.

5. Temperature Calibration Based on Si Raman

To check the efficiency of our heating stage, we utilize different clamps, including Ruthenium (Ru) probes, SUS340 clamping jig, and ceramic to mount the sample and calibrate the temperature based on the center position of Si Raman peaks. Figure S3, Supporting Information shows the relationship between the set temperature and the actual temperature of the heater over time. The center peak position of Si Raman mode as a function of temperature for both heating and cooling cycles using different clamping methods are shown in Figures S4–S6, Supporting Information. In all three cases, the center position of Si Raman peaks redshifts linearly as the temperature increases from room temperature up to 600 °C. We observe a high degree of consistency of the peak position between the heating and cooling cycles when the temperature is above 300 °C. However, the blueshift of Si peak becomes slow below 300 °C due to the slow heat dissipation process, though we take the measurements ≈15 min after the temperature sensor is stabilized. The temperature dependence of the first-order optical Raman mode of Si nanowires and bulk Si has been reported previously. In contrast to the inhomogeneous heating induced by laser excitation power, we employ a heating stage to achieve homogeneous heating of the devices. We refer to the temperature dependence of Raman scattering of the Si nanowires[51] to calibrate the temperature read from Si Raman peak, as shown in Figure S7, Supporting Information. When the chip is mounted by Ru probes, the temperature read from Si Raman peak is ≈345 °C at the heater setting temperature of 600 °C. Such a large temperature difference is probably due to the large thermal conductivity

of Ru ($\kappa \approx 151$ W mK^{-1}). We expected the heating efficiency to be improved when the chip is mounted by SUS340 clamping jigs with $\kappa \approx 15$–20 W mK^{-1}. We also insert a small piece of ceramic with a thermal conductivity of ≈3.8 W mK^{-1} between the SUS340 clamping jig and our chip. Though we expected a significant improvement in the heating efficiency, only minor improvements in the heating efficiency are observed. This may result from the multi-point contact between the ceramic piece and the chip; the large effective contact area accelerates the heat dissipation.

6. Conclusion

In summary, we have demonstrated the AlScN/SiC thin film micromachined resonators operating in high-temperature environments up to 600 °C. Macroscopic and microscopic vibrations in AlScN/SiC diaphragm resonators are investigated through a combination of ultrasensitive optical interferometry techniques and Raman scattering spectroscopy. By measuring the temperature dependence of multimode resonance, we obtain an average TCf of less than 1 ppm °C^{-1} from the first resonant mode of the resonator with d = 250 µm between 25 and 200°C, and an average TCf of –16 ppm °C^{-1} between 200 and 600 °C. The repeatable resonance results taken from the heating and cooling processes indicates that our AlScN/SiC diaphragm resonators can be operated at high temperature up to 600 °C, reliably and without any degradation. Raman results show that the turning point of the peak position of the LO mode of both 3C-SiC and AlScN occurs at almost the same temperature region where the turnover of TCf is observed. The results suggest that the microscopic vibrations in the crystal lattice and the macroscopic vibration of the diaphragm are naturally mediated by the residual strain inside the materials at varying temperatures. Our results provide insight in understanding how the variation of temperature affects the resonance behavior and material properties of AlScN/3C-SiC thin film resonators at both device and atomic levels.

7. Experimental Section

Device Fabrication: Single crystal n-type 3C-SiC (100) thin films with a thickness of 900 nm were grown on the Si (100) substrate by low-pressure chemical vapor deposition process. 1 µm thick AlScN with 20% Sc was then sputtered on the 3C-SiC/Si substrate. After the growth process, 500 nm thick Al_2O_3 thin film was sputtered on the backside and then patterned by the photolithography and wet etching to act as the hard mask for deep etching of Si. Circular diaphragms with diameters varying from 250 µm, 500 µm, 750 µm to 1 mm were designed and patterned on the Al_2O_3 mask. After that, the Si substrate with a thickness of around 650 µm was removed by deep reactive ion etching to form suspended diaphragms. The process was carefully controlled to maintain the anisotropic etching with steep sidewalls and stops when the embedded SiC layer was exposed.

Interferometric Resonance Measurements: The multimode resonances of the AlScN/SiC resonator were measured by using a laser interferometry system, as shown in Figure 1. An intensity-modulated 405 nm blue laser was utilized to photothermally excite resonances and a 633 nm He-Ne laser was focused on the device to detect the vibration. Dynamic interference happens between the light reflected by the vibrating membrane and that by the substrate surface below the suspended structure. A photodetector converts the time-varying optical interferometric signals into electrical signals and the frequency response is read out by a network analyzer. We regulate the temperature by using a customized heating and sensing system. First, the resonator is tested from room temperature up to 600 °C in 50 °C intervals for the ramp-up cycle. Subsequently, we gradually decrease the temperature in 50 °C intervals back to room temperature. At each temperature point, ≈15 min is waited for the temperature to stabilize, and we then take the resonance measurements. The laser-induced shift in resonance frequency due to the parasitic heating from the photothermal effect is minimal due to the wide bandgap of AlScN (≈5.5 eV for Sc at 20%, translating to a cutoff wavelength of 225 nm). Even if there is slight shift due to laser heating, it only produces a small offset of the entire frequency curve over the regulated temperature range, while the TCf remains accurate. To decouple the effect of parasitic heating on the resonance frequency, the power of the laser remains constant in all the measurements.

Raman Scattering Measurements: To trace the evolution of stress and the quality of the crystal at varying temperatures, Raman measurements were performed using a customized micro-Raman system integrated into the laser interferometry system. The 532 nm laser was focused on the AlScN thin film in a vacuum chamber using a 50 × microscope objective. Raman scattered light from the sample was collected in backscattering geometry and then guided to a spectrometer (Horiba iHR550) with a 2400 g mm^{-1} grating. The Raman signal was recorded using a liquid-nitrogen-cooled charge-coupled device.

Supporting Information

Supporting Information is available from the Wiley Online Library or from the author.

Acknowledgements

The authors thank the support from the Defense Threat Reduction Agency (DTRA) Basic Scientific Research Program under Grant HDTRA1-19-1-0035, the Army Research Office (ARO) under Grant W911NF-16-1-0340, and the Margaret A. Ross Fellowship from ECE, University of Florida.

Conflict of Interest

The authors declare no conflict of interest.

Data Availability Statement

The data that support the findings of this study are available from the corresponding author upon reasonable request.

Keywords

aluminum scandium nitride, harsh environment, high temperature, micro/nanoelectromechanical systems, micromachined transducers, resonators

Received: February 23, 2022
Revised: April 13, 2022
Published online:

[1] O. Solgaard, A. A. Godil, R. T. Howe, L. P. Lee, Y.-A. Peter, H. Zappe, *J. Microelectromech. Syst.* **2014**, *23*, 517.

[2] P. X.-L. Feng, D. J. Young, C. A. Zorman, in *MEMS/NEMS Devices and Applications* (Ed: B. Bhushan), *Springer Handbook of Nanotechnology*, Springer, Berlin, Heidelberg **2017**, Ch. 13, pp. 395–429.
[3] A. Nisar, N. Afzulpurkar, B. Mahaisavariya, A. Tuantranont, *Sens. Actuators B* **2008**, *130*, 917.
[4] W. J. Fleming, *IEEE Sens. J.* **2001**, *1*, 296.
[5] J. X. Wang, X. M. Qian, *Appl. Mech. Mater.* **2014**, *643*, 72.
[6] G. Esteves, S. D. Habermehl, P. J. Clews, C. Fritch, B. A. Griffin, *J. Microelectromech. Syst.* **2019**, *28*, 859.
[7] N. Marsi, B. Y. Majlis, A. A. Hamzah, F. Mohd-Yasin, *Energy Procedia* **2015**, *68*, 471.
[8] G. Kotzar, M. Freas, P. Abel, A. Fleischman, S. Roy, C. A. Zorman, J. M. Moran, J. Melzak, *Biomaterials* **2002**, *23*, 2737.
[9] A. Chaalane, R. Chemam, M. Houabes, R. Yahiaoui, A. Metatla, B. Ouari, N. Metatla, D. Mahi, A. Dkhissi, D. Esteve, *J. Phys.: Conf. Ser.* **2015**, *660*, 012137.
[10] T. G. Brown, *IEEE Sens.* **2003**, *2*, 753.
[11] W. Sui, X.-Q. Zheng, J.-T. Lin, B. W. Alphenaar, P. X.-L. Feng, *J. Microelectromech. Syst.* **2021**, *30*, 521.
[12] H. Chen, H. Jia, W. Liao, V. Pashaei, C. N. Arutt, M. W. McCurdy, C. A. Zorman, R. A. Reed, R. D. Schrimpf, M. L. Alles, P. X.-L. Feng, *Appl. Phys. Lett.* **2019**, *114*, 101901.
[13] J. K. Luo, Y. Q. Fu, H. R. Le, J. A. Williams, S. M. Spearing, W. I. Milne, *J. Micromech. Microeng.* **2007**, *17*, S147.
[14] K. Tonisch, V. Cimalla, Ch. Foerster, H. Romanus, O. Ambacher, D. Dontsov, *Sens. Actuators A* **2006**, *123*, 658.
[15] K. Kishi, Y. Ooishi, H. Noma, E. Ushijima, N. Ueno, M. Akiyama, T. Tabaru, *J. Eur. Ceram. Soc.* **2006**, *26*, 3425.
[16] C. M. Lin, W. C. Lien, V. V. Felmetsger, M. A. Hopcroft, D. G. Senesky, A. P. Pisano, *Appl. Phys. Lett.* **2010**, *97*, 141907.
[17] O. Zywitzki, T. Modes, S. Barth, H. Bartzsch, P. Frach, *Surf. Coat. Technol.* **2017**, *309*, 417.
[18] M. Akiyama, T. Kamohara, K. Kano, A. Teshigahara, Y. Takeuchi, N. Kawahara, *Adv. Mater.* **2009**, *21*, 593.
[19] O. E. Contreras, F. Ruiz-Zepeda, A. Dadgar, A. Krost, F. A. Ponce, *Appl. Phys. Express* **2008**, *1*, 061104.
[20] A. Tanaka, W. Choi, R. Chen, S. A. Dayeh, *Adv. Mater.* **2017**, *29*, 1702557.
[21] Y. Feng, H. Wei, S. Yang, Z. Chen, L. Wang, S. Kong, G. Zhao, X. Liu, *Sci. Rep.* **2014**, *4*, 6416.
[22] A. Pandey, S. Dutta, R. Prakash, R. Raman, A. K. Kapoor, D. Kaur, *J. Electron. Mater.* **2018**, *47*, 1405.
[23] B. A. Griffin, S. D. Habermehl, P. J. Clews, in *Proc. Sensors for Extreme Harsh Environments,* SPIE Sensing Technology and Applications, Baltimore, Maryland, United States **2014**.
[24] J. Komiyama, K. Eriguchi, Y. Abe, S. Suzuki, H. Nakanishi, T. Yamane, H. Murakami, A. Koukitu, *J. Cryst. Growth* **2008**, *310*, 96.
[25] M. Akiyama, T. Kamohara, K. Kano, A. Teshigahara, Y. Takeuchi, N. Kawahara, *Adv. Mater.* **2008**, *21*, 593.
[26] F. Ayazi, L. Sorenson, R. Tabrizian, in *Proc. Micro- and Nanotechnology Sensors, Systems, and Applications III*, Vol. *8031*, SPIE, May **2011**, pp. 371–383.
[27] H. P. Phan, T. K. Nguyen, T. Dinh, A. Iacopi, L. Hold, M. J. Shiddiky, D. V. Dao, N. T. Nguyen, *Adv. Eng. Mater.* **2018**, *20*, 1700858.
[28] M. Noraini, Y. M. Burhanuddin, Y. Faisal Mohd, Z. A. Hafzaliza Erny, H. Azrul Azlan, *Int. J. Nanoelectron.* **2020**, *13*, 113.
[29] M. Mehregany, C. A. Zorman, N. Rajan, C. H. Wu, *Proc. IEEE* **1998**, *86*, 1594.
[30] A. Qamar, H. P. Phan, T. Dinh, N. T. Nguyen, M. Rais-Zadeh, *Appl. Phys. Lett.* **2020**, *116*, 132902.
[31] W. B. Wang, Y. Q. Fu, J. J. Chen, W. P. Xuan, J. K. Chen, X. Z. Wang, P. Mayrhofer, P. F. Duan, A. Bittner, U. Schmid, J. K. Luo, *J. Micromech. Microeng.* **2016**, *26*, 075006.
[32] V. J. Gokhale, B. P. Downey, M. T. Hardy, E. N. Jin, J. A. Roussos, D. J. Meyer, presented at *Proc. IEEE 33th Int. Conf. Micro Electro Mech. Syst. (MEMS)*, Jan. **2020**.
[33] K. Y. Hashimoto, S. Sato, A. Teshigahara, T. Nakamura, K. Kano, *IEEE Trans. Sonics Ultrason.* **2013**, *60*, 637.
[34] C. M. Lin, T. T. Yen, V. V. Felmetsger, M. A. Hopcroft, J. H. Kuypers, A. P. Pisano, *Appl. Phys. Lett.* **2010**, *97*, 083501.
[35] M. Rinaldi, A. Tazzoli, J. Segovia-Fernandez, V. Felmetsger, G. Piazza, presented at *Proc. IEEE 25th Int. Conf. Micro Electro Mech. Syst. (MEMS)*, Paris, France, Feb., **2012**.
[36] G. Piazza, P. J. Stephanou, A. P. Pisano, *J. Microelectromech. Syst.* **2006**, *15*, 1406.
[37] M. Pozzi, M. Hassan, A. J. Harris, J. S. Burdess, L. Jiang, K. K. Lee, R. Cheung, G. J. Phelps, N. G. Wright, C. A. Zorman, M. Mehregany, *J. Phys. D: Appl. Phys.* **2007**, *40*, 3335.
[38] G. Wu, J. Xu, E. J. Ng, W. Chen, *J. Microelectromech. Syst.* **2020**, *29*, 1137.
[39] H. Suzuki, N. Yamaguchi, H. Izumi, *Acoust. Sci. Technol.* **2009**, *30*, 348.
[40] D. N. Talwar, L. Wan, C. C. Tin, Z. C. Feng, *J. Mater. Sci. Eng.* **2017**, *6*, 2169.
[41] V. Lughi, D. R. Clarke, *Appl. Phys. Lett.* **2006**, *89*, 241911.
[42] G. S. Chung, K. S. Kim, *Microelectron. J.* **2008**, *39*, 1405.
[43] Y. Tanaka, Y. Hasebe, T. Inushima, A. Sandhu, S. Ohoya, *J. Cryst. Growth* **2000**, *209*, 410.
[44] R. Deng, K. Jiang, D. Gall, *J. Appl. Phys.* **2014**, *115*, 013506.
[45] A. L. Mock, A. G. Jacobs, E. N. Jin, M. T. Hardy, M. J. Tadjer, *Appl. Phys. Lett.* **2020**, *117*, 232107.
[46] Y. Song, C. Perez, G. Esteves, J. S. Lundh, C. B. Saltonstall, T. E. Beechem, J. I. Yang, K. Ferri, J. E. Brown, Z. Tang, J. P. Maria, *ACS Appl. Mater. Interfaces* **2021**, *13*, 19031.
[47] V. Lysenko, D. Barbier, B. Champagnon, *Appl. Phys. Lett.* **2001**, *79*, 2366.
[48] W. L. Zhu, J. L. Zhu, S. Nishino, G. Pezzotti, *Appl. Surf. Sci.* **2006**, *252*, 2346.
[49] M. Balkanski, R. F. Wallis, E. Haro, *Phys. Rev. B* **1983**, *28*, 1928.
[50] Y. Chen, B. Peng, B. Wang, *J. Phys. Chem. C* **2007**, *111*, 5855.
[51] S. Khachadorian, H. Scheel, A. Colli, A. Vierck, C. Thomsen, *Phys. Status Solidi B* **2010**, *247*, 3084.